Identification of plasma environments within the terrestrial magnetotail and its global structure from the Magnetospheric Multiscale Mission

Tien Vo[1,2], Robert Ergun[1,2,3], Maria Usanova[1], and Alexandros Chasapis[1]

[1]Laboratory for Atmospheric and Space Physics, University of Colorado
[2]Department of Physics, University of Colorado
[3]Department of Astrophysical and Planetary Sciences, University of Colorado

June 30, 2023

Identification of plasma environments within the terrestrial magnetotail and its global structure from the Magnetospheric Multiscale Mission

T. Vo[1,3], R. E. Ergun[1,2], M. E. Usanova[1], and A. Chasapis[1]

[1] Laboratory for Atmospheric and Space Physics, University of Colorado, Boulder, CO, USA
[2] Department of Astrophysical and Planetary Sciences, University of Colorado, Boulder, CO, USA
[3] Department of Physics, University of Colorado, Boulder, CO, USA

Key Points:

- Inner-magnetotail environments are statistically identified with background plasma conditions and their global 3D structure is studied.
- Warping effects attributed to changes in the Earth's dipole tilt angle leads to an apparent dawn-dusk asymmetry during the summer months.
- We utilize a large volume of MMS data with partial plasma moments calculated from low-energy plasma and energetic particle instruments.

Corresponding author: Tien Vo, `Tien.Vo@lasp.colorado.edu`

Abstract

Using MMS orbits in the Earth's magnetotail from 2017 to 2020, plasma conditions and the 3D spatial structure of inner-magnetotail plasma environments (with a focus on the plasma sheet) are studied with different approaches. Threshold conditions for distinguishing the plasma sheet, plasma sheet boundary layers, and lobes are derived from the statistical properties of background plasma parameters. Our results support previous studies that employed similar methods using Cluster data. However, stronger currents are observed in both the lobes and plasma sheet, likely due to the smaller spacecraft separation ($\lesssim 70\,\mathrm{km}$) that can resolve thin electron-scale currents. Threshold conditions are used together with magnetic field and electric field measurements to image the spatial structure of the plasma sheet. Results are in good agreement with a global neutral sheet model based on solar wind conditions and magnetospheric configurations. Furthermore, the Earth's dipole tilts towards the Sun around June solstice, which warps the magnetotail as much as ~ 2–$4\,\mathrm{R_E}$ in Z GSM. This warping effect is relaxed towards September equinox. Consequently, as MMS travels through the magnetotail from dawn to dusk during this period, there is an apparent dawn-dusk asymmetry in plasma conditions between June and September. Kink-like flapping waves and IMF twisting are other mesoscale processes attributed with a few R_E of flaring near the flanks. These findings reveal important insights into the mesoscale structure and dynamics of the magnetotail.

Plain Language Summary

Data from four years of observations by NASA's MMS mission are used to statistically identify distinctive regions within the Earth's magnetospheric tail. This study reveals insights into the spatial structure of this "magnetotail" and seasonal variations attributed with changes in the Earth's magnetic field configurations, particularly those of the orientation of the Earth's dipole. Our results agree with reported findings from ESA's Cluster mission. However, certain aspects unique to MMS lead to some improved measurements and features relating to MMS orbital design. The presented results are highly beneficial to future large statistical studies with MMS data.

1 Introduction

Situated at the nightside of the Earth's magnetosphere, the magnetotail can stretch as far as $\sim 10^3$ Earth radii (R_E) (Dungey, 1965; Cowley, 1991) and can exceed $30\,\mathrm{R_E}$ in radius (Coroniti & Kennel, 1972; Shukhtina et al., 2004). Driven by interactions with the solar wind and the interplanetary magnetic field (IMF) as well as changes in geomagnetic configurations and plasma conditions, it plays a central role in magnetospheric dynamics from global to kinetic scales. Therefore, to understand the multiscale dynamics within the magnetotail, there has been great interest to identify its complex structure and plasma conditions.

From global to meso-scales, the magnetotail is subjected to distinct types of deformation, three of which are known as flapping, twisting, and warping (Dayeh et al., 2015). Solar wind directional changes can cause it to flap either steadily in the north-south direction, or drive kink-like waves propagating towards the flanks (Lui et al., 1978; Sergeev et al., 2003; Zhang et al., 2005; Gao et al., 2018). The flapping and the waves have periods on the order of 1–10 minutes with wavelengths of $1–4\,\mathrm{R_E}$ (Rong et al., 2018; Wang et al., 2019). Non-zero IMF B_y can apply a torque and twist the tail as high as $50°$ about the Sun-Earth line (Owen et al., 1995; Tsyganenko, 1998). Due to the $\sim 11°$ tilt of the Earth's dipole axis with respect to its rotational axis (Amit & Olson, 2008), the magnetotail is periodically displaced $\sim 1–2\,\mathrm{R_E}$ above and below the equatorial plane (Hammond et al., 1994) with a hinge radius of $\sim 10\,\mathrm{R_E}$ (Tsyganenko & Fairfield, 2004). Under these effects, the tail shape is extremely complex and variable on time scales from a few minutes to many days and spatial scales up to many Earth radii.

There are several distinct plasma environments in the magnetotail. Boundary layers at the flanks can bring magnetosheath plasma into the inner magnetosphere via mixing instabilities (e.g. Otto & Fairfield, 2000; Fairfield et al., 2000; Nykyri et al., 2006; Johnson et al., 2014). In the middle of the tail, a plasma sheet (PS), which is a few $\mathrm{R_E}$ in thickness under normal conditions (Russell & McPherron, 1973; McComas et al., 1986; Sanny et al., 1994; Zhou et al., 1997), contains high-beta plasma and low equatorial magnetic field (Baumjohann et al., 1989). To the contrary, the northern and southern lobes enclosing the PS are often characterized by low-beta plasma and high equatorial magnetic field, predominantly pointing sunward or antisunward. Separating the PS and the lobes, the plasma sheet boundary layers (PSBLs) mix hot and cold plasmas from these two environments (Eastman et al., 1984) and often display signatures of nonlinear kinetic structures (Cattell et al., 1986; Nakamura et al., 2004; Ergun et al., 2009; Malaspina et al., 2015; Tong et al., 2018). Embedded within the PS is a neutral sheet (NS), often characterized as the null point of the equatorial magnetic field. The NS is the locus of many explosive geomagnetic activities during substorms (Sitnov et al., 2019, and references therein) which include, for example, kinetic instabilities, magnetic reconnection, locally generated turbulence, particle energization, etc (Zimbardo et al., 2010; Sitnov & Schindler, 2010; Liu et al., 2014; Ukhorskiy et al., 2017; Chen et al., 2019; Ergun et al., 2020a, 2020b, 2022; Usanova & Ergun, 2022).

The complex evolution of mesoscale dynamics and kinetic-scale structures often make identifying the various plasma environments a non-trivial task. Previous attempts to identify plasma environments and their spatial variations in the inner magnetotail have included a number of different methods. Combining decades of data, multi-mission studies (Hammond et al., 1994; Tsyganenko & Fairfield, 2004; Dayeh et al., 2015; Xiao et al., 2016) have imaged the neutral sheet under twisting and warping effects by observing the sign of magnetospheric B_x, from which global models are constructed. Multi-spacecraft missions, e.g. Cluster (Escoubet et al., 2001) and THEMIS (Angelopoulos et al., 2008), allow for timing analysis, often used to study the flapping motion (Runov et al., 2005, 2009). Most commonly, statistical threshold conditions based on averaged background parameters such as the plasma beta, number density, current density, magnetic field and/or plasma flow are used to distinguish the NS, PS, PSBL, and lobe (Baumjohann et al., 1988; Angelopoulos et al., 1994; Åsnes et al., 2008; Boakes et al., 2014). Assuming a certain time scale of the magnetic fluctuations, threshold conditions can also be defined based on magnetometer data alone to distinguish the lobe and PS (Coxon et al., 2016). When the threshold approach fails, the outer layer of the PS and PSBL may be determined on a case-by-case basis by analyzing beam-like populations in the 3D distribution function (Grigorenko et al., 2012) or ionospheric photoelectrons (Pedersen et al., 1985; Baumjohann et al., 1988).

The Magnetospheric Multiscale mission (MMS), launched in 2015, is a NASA four-spacecraft mission (Burch et al., 2016) that targets electron-scale magnetospheric physics, building upon the success of Cluster. Capable of higher time resolution and higher accuracy electromagnetic field and particle measurements, MMS has the potential to reinforce past studies of global models, threshold conditions, and kinetic-scale properties.

As apparent from previous experiences, it is challenging to achieve a definitive identification of the inner-magnetotail plasma environments at any given time. Nevertheless, knowledge of mesoscale factors and background parameters from MMS data can provide insights into the magnetotail configuration at various scales. We remark that identifying plasma regions and boundaries is essential to a systematic statistical study of kinetic-scale magnetotail physics.

In this paper, we utilize a large volume of MMS observations to investigate the properties of magnetotail plasma environments through a few different approaches, with a focus on the plasma sheet. Statistically, we derive threshold conditions based on background plasma conditions to distinguish different environments. Results are discussed in comparison with those from a previous study using Cluster data (Boakes et al., 2014). Furthermore, the large volume of data allows for enough spatial coverage to image the global structure of the neutral sheet (i.e. through magnetic field measurements similar to Tsyganenko & Fairfield, 2004; Xiao et al., 2016). The structure of the NS based on B_x will be compared with that of the PS identified from the threshold approach, and the NS model fitted by Xiao et al. (2016). Since the NS is embedded within the PS, we show that all of these approaches (threshold, imaging, modeling) generally agree, thereby revealing insights into both the statistical properties of background plasma conditions and the spatial variations of the NS/PS within the magnetotail. For example, since MMS always visits the magnetotail from June solstice to September equinox (correspondingly, from the dawn to dusk sectors in GSM coordinates), observations of the PS spatial structure reveal that warping effects are prominent around June and insignificant around September, resulting in an apparent dawn-dusk asymmetry in plasma conditions. Our data also feature the combination of partial plasma moments from low-energy plasma and energetic particle instruments, the technicality and motivation for which are presented in this paper.

This paper is organized as follows. In Section 2, we describe relevant details of MMS instrumentation. In Section 3, we describe our dataset, which is compiled from a broad array of MMS instruments measuring fields and particles, where we also present the combined plasma moments and the motivation for their consideration. In Section 4, we discuss the exclusion of outer magnetotail environments and present the properties of background plasma conditions in the inner magnetotail. In Section 5, we examine the 3D global structure of the neutral sheet and plasma sheet using the threshold, imaging, and modeling approaches. Finally, we discuss the implications of these results and provide concluding remarks in Section 6.

2 Instrumentation

A broad array of MMS instruments are used enable and optimize statistical magnetotail studies of the electromagnetic field, particle properties, and their correlation. While the present paper only concerns with statistical, mesoscale quantities, we recognize that the large volume of data considered here also can be generically advantageous for future large-scale studies of kinetic physics in the magnetotail.

The four identical MMS spacecrafts travel in a tetrahedral formation with a highly eccentric, near-Earth-equatorial orbit with an initial apogee of $12\,\mathrm{R_E}$ and a perigee of roughly $1.2\,\mathrm{R_E}$ (Fuselier et al., 2016). The natural (inertial) orbital precession is small, but as the Earth orbits the Sun, the apogee rotates between the subsolar region and the magnetotail in roughly one year. Annually, magnetotail observations occur for MMS primarily in the summer months between June solstice and September equinox. To maximize encounters with the neutral sheet during these seasons, the night-side apogee was raised to $25\,\mathrm{R_E}$ in early 2017 and subsequently to $28\,\mathrm{R_E}$ in 2019 (Tedla et al., 2018). Throughout the magnetotail, MMS instruments operate in two data acquisition rates (fast survey and burst). Fast survey data provide continuous coverage, and burst data are selected short-duration intervals of high time-resolution measurements. In this paper, we use fast survey data from 2017 to the end of 2020 to optimize statistical observations of magnetotail processes occurring between 12 and $28\,\mathrm{R_E}$.

In fast survey mode, the FIELDS investigation provides measurements of the DC magnetic field and DC electric field in resolutions of 62.5 ms and 31.25 ms through the Fluxgate Magnetometers (FGM) and Electric Double Probes (EDP) instruments (Torbert et al., 2016; Russell et al., 2016; Ergun et al., 2016). At apogee, the tetrahedral formation is targeted to have a geometric quality factor $Q \geq 0.7$ ($Q = 1$ being a perfect tetrahedron) and an average spacecraft separation of 40 km, enabling measurements of field gradients on several electron scales (Fuselier et al., 2016). Particularly, the current density $\mathbf{J} = \boldsymbol{\nabla} \times \mathbf{B}/\mu_0$ can be estimated using the curlometer technique (Paschmann & Daly, 1998; Dunlop et al., 2021). Simultaneous multi-spacecraft measurements also allow for calculations of barycentric quantities so that, for example, plasma dissipation measures such as $\mathbf{J} \cdot (\mathbf{E} + \mathbf{u} \times \mathbf{B})$ (Zenitani & Hoshino, 2005; Ergun et al., 2018) or $(\mathbf{P} \cdot \boldsymbol{\nabla}) \cdot \mathbf{u}$ (Chasapis et al., 2018; Yang et al., 2022) may be examined.

The Fast Plasma Investigation (FPI) samples plasma populations in the low-energy range from 10 eV to 30 keV with time resolutions of 30 ms for electrons and 150 ms for ions (Pollock et al., 2016). FPI instruments utilize top-hat electrostatic analyzers, forming 512 distributed field-of-views (FOVs) over the full 4π-sr solid angle, each measuring 32 energy channels. The fast survey FPI data products used in this study are 3D electron and ion distribution functions that are integrated on-board high time-resolution measurements and reduced to 4.5-s resolution. FPI also provides partial plasma moments (associated with its capable energy range) integrated in velocity space from the 4.5-s products.

At the high-energy range, the Energetic Particle Detector (EPD) investigation comprises the Fly's Eye Energetic Particle Sensor (FEEPS) and Energetic Ion Spectrometer (EIS) instruments, utilizing micro-channel plates and solid-state detectors to sample energetic particles in the range of 60–500 keV (Mauk et al., 2016; Blake et al., 2016). For better ion data availability and energetic electron measurements, we utilize FEEPS data in this study. On each spacecraft, two FEEPS instruments are mounted 180° apart on the spin plane, providing 9 electron FOVs (5 operating in fast survey) and 3 ion FOVs, each measuring energy with 16 channels. Although this configuration provides instantaneous measurements of the particle distribution over a 3π-sr solid angle, the main data products are electron and ion energy-angle distributions, averaged in 2.5-s resolution by means of rotation. As opposed to the full 3D distribution functions measured by FPI at low energies, the most reliably available of the FEEPS measurements are spin-scanned, omni-directional distribution functions. Therefore, the partial plasma moments that can be calculated from FEEPS data are more limited than those from FPI data.

3 Methodology and Data

In the previous section, it is clear that low-energy ($\lesssim 30$ keV) and high-energy ($\gtrsim 60$ keV) particles are measured by MMS with instruments that have quite distinct techniques (FPI and FEEPS, respectively), resulting in different time resolutions, angular coverages, and an energy-coverage gap of about 30 keV. Therefore, it is not trivial how partial plasma moments may be calculated (in the high-energy range) and combined from the two instruments. While the combination of partial plasma moments has been applied for previous capable missions such as THEMIS (Angelopoulos et al., 2008; Hietala et al., 2015; Shustov et al., 2019) and Cluster (Haaland et al., 2010), it has not been routinely performed for MMS and is often the constraining factor in previous studies, particularly those investigating ion properties. For example, Artemyev et al. (2021) acknowledges the importance of contributions of 100-keV ions to the plasma moments in the magnetotail, but because of the aforementioned constraint, these contributions are extrapolated using THEMIS data by a scaling argument instead of direct calculations. In the following, we provide another motivation for the necessity of combined plasma moments in the magnetotail through a case study. At the same time, we present a demonstration of our methodology in estimating the contributions of energetic particles to the plasma moments. Technical details of this combination are specific to MMS data products and discussed at length in Appendix A.

Consider a well-documented observation of a strongly turbulent, retreating reconnection X-line in the magnetotail in Fig. 1 (Ergun et al., 2018, 2020a, 2020b). In (a–c), an ion flow reversal occurs around 07:29, together with strong electromagnetic fluctuations persisting about 15 minutes, in which many intermittent structures are found such as double layers, magnetic holes, electron phase-space holes, and thin current sheets. At the same time, increases in energetic ion and electron energy fluxes are observed in (d) and (e). The energy fluxes at some time before, during, and after the turbulent event (denoted in (a–h) with vertical blue, green, and red lines) are also plotted in (i) and (j). The particle distributions in (d–e) and (i–j) are omni-directional and contain both measurements from FPI (below the lower-energy, magenta dashed line) and FEEPS (above the higher-energy dashed line). FEEPS measurements are interpolated to FPI resolution.

From past statistical studies (Huang et al., 2020; Chong et al., 2022), it is reasonable to assume that the plasma bulk flow rarely surpasses FPI capabilities (about 2,000 km/s for ions and 100,000 km/s for electrons). So the contribution from thermal (low-energy) particles to the plasma moments can be calculated from the FPI 3D distribution functions, correctly accounting for drifted particles. Subsequently, the non-thermal contribution may be considered isotropic and calculated from omni-directional distribution functions as detailed in Appendix A. However, this calculation is limited to directionless quantities, such as the number density and scalar pressure. Most clearly seen in (i–j), the energy-

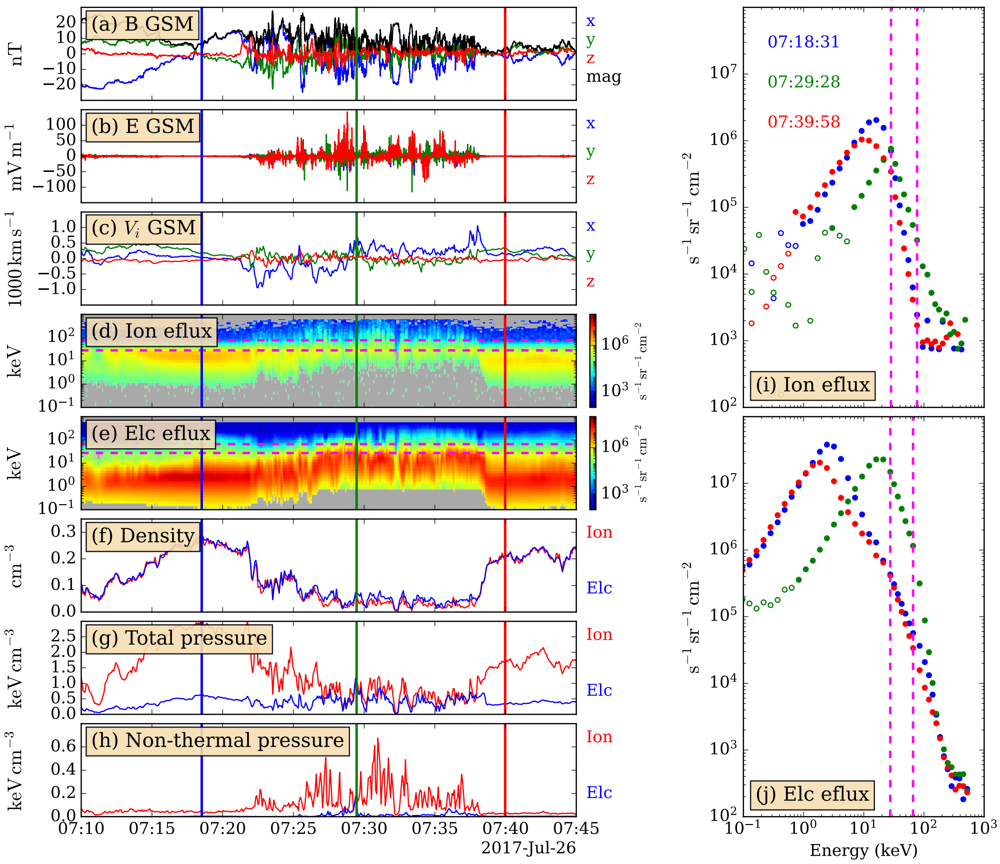

Figure 1. Example of FPI-FEEPS combined moment calculations for a strong turbulent reconnection event in the magnetotail. (a) Barycentric magnetic field. (b) Barycentric electric field. The rest of the panels show data from MMS1. (c) Ion velocity. (d) Combined omni-directional ion energy flux. (e) Combined omni-directional electron energy flux. (f) Combined ion (red) and electron (blue) density. (g) Combined ion and electron total pressure. (h) Pressure contribution of non-thermal, energetic (larger than FPI energy threshold) particles. In (a-h), the blue, green, red vertical lines are times before, during, and after the turbulent event. (i) The ion energy flux during vertical snapshots in (a-h). (j) Similarly, snapshots in electron energy flux. Hollow markers are noise-level or background measurements. The dashed magenta lines [horizontal in (d) & (e), vertical in (i) & (j)] denote the extrapolated energy gap between FPI and FEEPS. There are 5 extrapolated points in that gap.

coverage gap (between the dashed lines) may contain a significant contribution to the plasma moments. Thus, we extrapolate the distribution function in this gap from FPI and FEEPS measurements and include its contribution in the non-thermal moment calculations (see Appendix A). In (f–h), we show the total (thermal + non-thermal) number density, total pressure, and non-thermal pressure.

In this event, one significant feature emphasized by the Ergun et al studies is that the reconnection inflow does not resupply particles from the lobe as fast as plasma sheet particles are depleted by the outflow, which results in a density drop in the turbulent region in (f) and the depletion of low-energy particles in (i–j). What we emphasize here is that because of this depletion of low-energy particles, when comparing (g) and (h), the contribution of non-thermal and/or energetic ions to the total pressure (characteristic energy density $P_s = nk_BT_s$ of species s) is on the order of 10 % and can be as high as 50 %. While most electrons are within the thermal (FPI) energy range, there can also be a significant fraction of non-thermal electrons ($\sim$ 10–20 % of total electron pressure) in this type of events. Since the frequency of events similar to the one shown in Fig. 1 is not yet established, pressure and temperature calculations solely based on the FPI instrument in the magnetotail may be underestimated for these occurrences. Therefore, it may be crucial for statistical studies of particle energization in the magnetotail to consider plasma moments combined from both FPI and FEEPS.

The calculation of combined plasma moments above requires that there is simultaneous availability from both particle instruments. We also require that electromagnetic field observations (from FGM and EDP) are available to enable future statistical studies of the correlation between field and particle observations. Such a study will be able to establish the statistical occurrence between turbulence, reconnection, and particle energization events such as the example in Fig. 1.

For this study, we have compiled continuous intervals (no significant time gap; duration from minutes to hours) of good availability from the magnetic field, electric field, low-energy plasma, and energetic particle instruments during MMS magnetotail seasons from 2017 to 2020. Additionally, 1-minute averaged solar wind conditions are obtained from the OMNI dataset (King & Papitashvili, 2005), which is used to correlate the magnetotail dynamics with solar wind conditions. In total, there are 437,728,300 field (FGM resolution) and 6,078,827 particle (FPI resolution) data points, amounting to about 316 continuous days of observation. Details of compilation of these intervals are highly technical and are laid out in the Supporting Information (SI). The principal conditions are listed below.

1. $X < 0$
2. $R \geq 12R_E$
3. $Q \geq 0.75$
4. No periods of thruster firing, EDP probe saturation, shadow spikes, or bad bias settings.
5. FGM, EDP available from MMS(1–4).
6. FPI, FEEPS available from MMS1.
7. Interval at least 1-minute long.

Above, $\mathbf{R} = (X, Y, Z)$ is the spacecraft position in GSM. While most global models of the neutral sheet, one of which is later on analyzed and compared, are fitted in aberrated GSM (AGSM), we have found little difference between GSM and AGSM in our results. Thus, we retain the usage of GSM for all coordinates in subsequent sections. Conditions (3) and (5) ensures that the barycentric electromagnetic fields and the curlometer current density may be accurately estimated. (4) ensures intervals of adequate EDP data for analysis. (6) ensures the partial plasma moments can always be combined. (7) enforces that the intervals are adequately long for spectral analysis.

4 Properties of the magnetotail background plasma conditions

In this section, we first distinguish the inner magnetotail from the solar wind and flank-side boundary layers, the properties of which are outside the scope of the present paper. Then, we present the statistical properties of the inner-magnetotail plasma conditions and compare our results with those in Boakes et al. (2014), hereby referred to as B14. Also, as done in B14, threshold conditions for the PS, PSBL, and lobe are derived based on the statistical properties of the plasma.

4.1 Exclusion of solar wind and flank-side boundary layers

Fig. 2 shows the X–Y distribution of (a) the coverage of MMS trajectory, (b) the ion density n_i, (c) the electron temperature T_e, and (d) the standard deviation of the

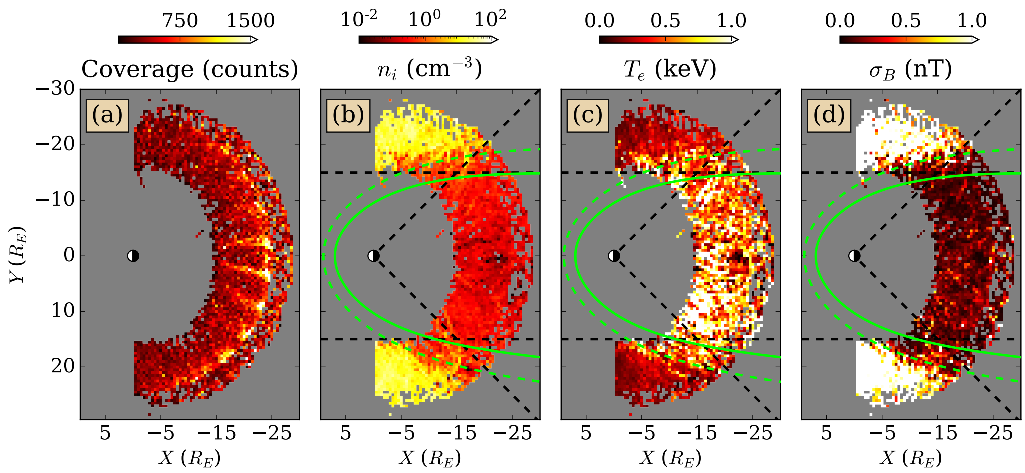

Figure 2. Spatial distribution in the X–Y plane of (a) MMS coverage during tail seasons in 2017–2020, (b) the ion density n_i, (c) the electron temperature T_e, and (d) standard deviation of the magnetic field σ_B. The lime curves are a 5° (clockwise) tilted magnetopause model (Lin et al., 2010) constructed with zero IMF B_z and total solar wind pressure of 5 nPa (dashed) and 20 nPa (solid). Dashed black lines denote $|Y| \leq 15\,\mathrm{R_E}$ and $|Y| \leq |X|$. The color scales are chosen to saturate solar wind values to also reveal typical plasma values in the tail.

magnetic field σ_B (over a 5-s moving window). In the magnetotail, the electron density (n_e) measurement is more accurate than n_i. However, the reverse is true in the solar wind. Here, we use n_i to reveal the differences between the solar wind and the magnetotail. Later, we use n_e when characterizing the magnetotail. 3D histograms are calculated with $0.5\,\mathrm{R_E} \times 0.5\,\mathrm{R_E} \times 0.5\,\mathrm{R_E}$ cubic bins then averaged over the Z direction, except for (a), which is summed instead. Hereafter, all data (e.g. the magnetic field, electric field, and current density) are averaged over a 5-s moving window and subsequently down-sampled to FPI resolution (4.5 s) so that particle and field measurements can be compared. Thus, in (a), each count represents a 5-s observation and the total count in each bin represents the dwell time of MMS spacecrafts. 3D bins that have lower than 100 counts are excluded as they may not be statistically representative.

In (a), the dwell time is not uniform. The highly-eccentric orbit has MMS spend more time near the apogee to maximize the chance of observing the diffusion region at reconnection sites (Fuselier et al., 2016). However, bins that have statistically significant counts are distributed over a large and uniform enough area so that the spatial distribution of plasma parameters can be studied. Most notably in (b–d), the solar wind is observed (as saturated colors) at $|Y| \gtrsim 15\,\mathrm{R_E}$, where averaged values are $n_i \sim 10$–$100\,\mathrm{cm}^{-3}$, $\sigma_B \sim 1$–$5\,\mathrm{nT}$, and $T_e \sim 0.01$–$0.1\,\mathrm{keV}$. In contrast, plasma parameters in the inner magnetotail are generally 1–2 orders of magnitude smaller, where $n_i \sim 0.1$–$1\,\mathrm{cm}^{-3}$, $\sigma_B \sim 0.1$–$0.5\,\mathrm{nT}$, and $T_e \sim 1\,\mathrm{keV}$. Fig. 2 shows that in general, background plasma parameters such as the density, temperature, and magnetic field fluctuations are distinctive between the inner and outer magnetotail. Thus, we can use these differences to statistically exclude regions more likely associated with the solar wind or flank-side boundary layers.

OMNI solar wind observations during MMS magnetotail seasons indicate average IMF $B_z \sim 0$ and total pressure $P_{\mathrm{sw}} \sim 1$–$5\,\mathrm{nPa}$. We use these parameters to construct an asymmetric magnetopause model (Lin et al., 2010), plotted as dashed ($P_{\mathrm{sw}} = 5\,\mathrm{nPa}$) and solid ($P_{\mathrm{sw}} = 20\,\mathrm{nPa}$) lime curves in (b–d). Details about the average OMNI observations and the Lin10 model are provided in Appendix B. The dashed curve agrees well with the change in plasma parameters. Thus, to be conservative when eliminating boundary layers, we define the inner magnetotail as the region bounded by the solid lime curve. In subsequent sections, all statistical results are obtained with data located strictly within this region.

For comparison, previous statistical studies have typically constrained the inner magnetotail region either with (i) $|Y| \leq |X|$ (Ergun et al., 2015) or (ii) with a threshold $|Y| \leq Y_0$ (Boakes et al., 2014; Chong et al., 2022). These two constraints are plotted as dashed black lines in (b–d). On a closer look, they are all somewhat equivalent conditions. (i) tends to work for smaller radial distances $R \leq 12\,\mathrm{R_E}$, and (ii) is good for small enough threshold Y_0, although the popular choice $Y_0 = 15\,\mathrm{R_E}$ may include some mixed plasma data.

4.2 Identification of inner tail plasma environments

Fig. 3 shows the statistical profile of background plasma parameters in terms of the ion beta $\beta_i = P_i/(B^2/2\mu_0)$, where P_i is the ion pressure. For comparison, it is plotted in the same format as Figure 1 in B14. (a) and (b) show the current density components parallel ($J_\parallel$) and perpendicular ($J_\perp$) to the background magnetic field. (c) shows the electron density n_e, and (d) shows the equatorial magnetic field B_{xy}. Due to the solenoidal condition ($\boldsymbol{\nabla} \cdot \mathbf{B} = 0$), the noise level of the curlometer currents in (a–b) can

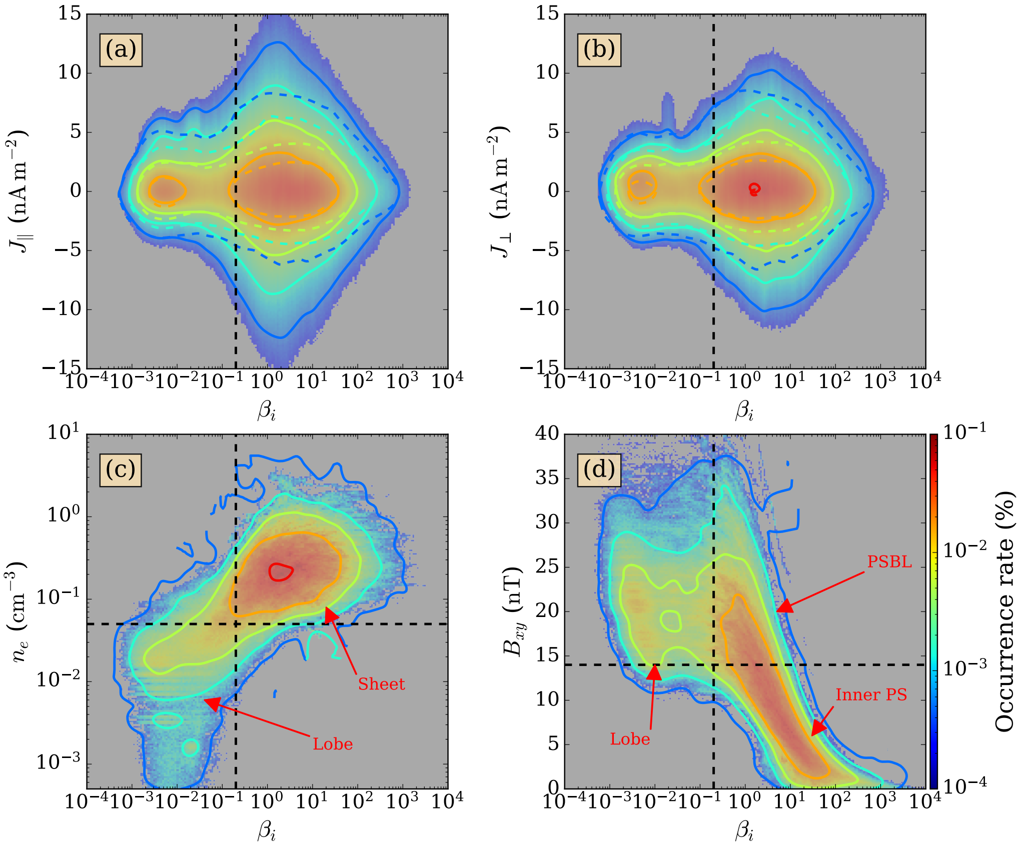

Figure 3. Occurrence rates of (a) the parallel current density $J_\parallel$, (b) the perpendicular current density $J_\perp$ (in the cross-tail direction, $\hat{\mathbf{z}} \times \mathbf{B}$), (c) the electron density n_e, and (d) the equatorial magnetic field B_{xy} in terms of the ion plasma beta β_i. Solid lines are contours of the colored distributions. In (a) and (b), the overplotted colored dashed lines are contours of the noise estimation of the curlometer current, $\nabla \cdot \mathbf{B}/\mu_0$. In all panels, the vertical dashed line denotes $\beta_i = 0.2$. In (c), the horizontal dashed line is the FPI 1-count level $n_e = 0.05\,\mathrm{cm}^{-3}$. In (d), the horizontal dashed line denotes $B_{xy} = 14\,\mathrm{nT}$.

Table 1. Threshold conditions distinguishing tail plasma environments derived from Fig. 3.

Plasma environment	Condition
Lobe	$\beta_i < 0.2$
Plasma sheet	$\beta_i \geq 0.2$ & $B_{xy} \leq 14\,\mathrm{nT}$
Plasma sheet boundary layer	$\beta_i \geq 0.2$ & $B_{xy} > 14\,\mathrm{nT}$

be estimated as $J_{\mathrm{noise}} = \boldsymbol{\nabla} \cdot \mathbf{B}/\mu_0$. In these panels, we have overplotted the contours of J_{noise} for comparison with the current amplitude. At a given color, currents larger than noise are measured if the solid line is wider than the dashed line.

In general, the features in this plot are consistent with the Cluster study. Most clearly in all panels, there are two distinct populations separated by β_i. The lobe-like population has low density ($n_e \sim 0.01\,\mathrm{cm}^{-3}$), low beta ($\beta_i \sim 0.01$), and high equatorial magnetic field ($B_{xy} \sim 20\,\mathrm{nT}$). In contrast, the plasma sheet-like population has high density ($n_e \sim 0.1\,\mathrm{cm}^{-3}$), high beta ($\beta_i \sim 1$), and low field ($B_{xy} \sim 5\,\mathrm{nT}$). One note of caution is the region of low electron density. The FPI instrument has a large uncertainty if the electron density is below $0.05\,\mathrm{cm}^{-3}$ [horizontal dashed line in (c)]. However, noise and background in the combined FPI-FEEPS distribution function has been treated carefully in the low-density region such that the accuracy is improved (see Appendix A for details). In subsequent sections, the threshold conditions for the plasma sheet are the main subject of study, where the density is typically higher than the FPI threshold.

To systematically determine the thresholds, B14 used changes in the current and electron densities with respect to β_i to define the PS/lobe separation and similarly, the statistical spread in B_{xy} to distinguish between the PSBL and the outer/inner regions of the plasma sheet. The threshold conditions were then reported annually. However, we deem it unnecessary for that level of detail in this study. It suffices to define by visual inspection the threshold conditions as tabulated in Table 1 and annotated in Fig. 3. We also make no attempt to distinguish the inner PS from the outer PS as done in B14. In general, our thresholds are all consistent with averages from the yearly results in B14. The beta threshold is slightly higher (by a factor of 2), most probably due to the usage of combined plasma moments (only partial moments with energies $\lesssim 40\,\mathrm{keV}$ were used in the B14 study).

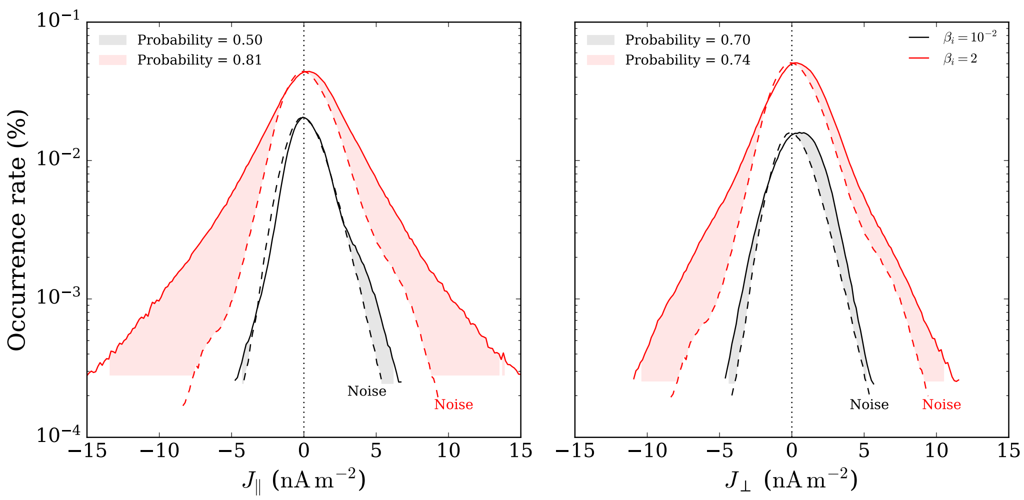

Figure 4. Vertical cuts of the statistical distribution of the currents in Fig. 3(a–b) at $\beta_i = 10^{-2}$ (in black) and $\beta_i = 2$ (in red). The corresponding dashed lines with the same colors are the noise estimation J_{noise}. The shaded areas are those where more occurrence is observed at a given amplitude than the noise estimation. The probability of these observations based on the shown conditional distribution functions (on β_i) is provided in the legends (shaded area versus total area under the solid lines).

In (a) and (b), the average current amplitude in the PS is consistent with results in B14 (0.5–2 nA/m^2). However, a difference among our results is in the lobe (low-beta region). B14 only observed noise in this region ($J \sim 0.5$ nA/m^2). But the wider (green/blue) contours than J_{noise} show that there are detections of statistically significant lobe currents above the noise level. To better visualize this difference, Fig. 4 shows vertical cuts of these panels at $\beta_i = 10^{-2}$ (black) and $\beta_i = 2$ (red). The occurrence rate of high-beta currents is higher than those with low β_i. The shaded regions indicate that there are “wings” in the probability distribution functions (PDFs) that is more significant than the statistics of noise (dashed lines). At any occurrence rate below 2×10^{-3} % for low β_i, the detected current amplitudes are higher than the estimated noise, which means wider contours in Fig. 3. Finally, to show the partition between noise-level currents (in the “core” of the PDFs) and non-noise currents (in the wings), we calculate the probability of the latter (see the figure legends) and discover that at least half of the observations are not noise. That said, the low overall occurrence rate indicates that their detection is not common.

In the magnetotail, the typical Cluster spacecraft separation is 1000s of km (Escoubet et al., 2001), which is comparable to the average ion inertial length. About $\sqrt{m_i/m_e} \sim 40$ times smaller, the typical electron inertial length is $\sim 20\,\mathrm{km}$. Since the target of MMS is electron physics, 97 % of the dataset has spacecraft separation $\leq 70\,\mathrm{km}$ (not shown). As a result, intense electron-scale currents are resolved in MMS data, but may be underestimated in Cluster data due to the linear spatial interpolation in the curlometer technique (Paschmann & Daly, 1998). . Therefore, we hypothesize that the presence of significant lobe currents in our statistics is due to the smaller spacecraft separation. Future studies are necessary to reveal their origin and properties. Overall, these results still provide strong support of Cluster observations from the MMS mission, with an improvement on current density measurements.

5 Global structure of the magnetotail plasma sheet

In this section, we investigate the three-dimensional global structure of the plasma sheet. As mentioned in Section 1, the magnetotail is influenced by processes such as flapping, twisting, and warping. Therefore, the plasma sheet may be highly deformed on mesoscales. In that case, it is interesting to study the spatial variations of the background plasma conditions, based on which the PS threshold condition is established in Table 1. From solar wind observations in Appendix B, the average IMF B_y is around $2\,\mathrm{nT}$ with near-zero IMF B_z, suggesting that the twisting angle should not be significant for radial distances smaller than $30\,\mathrm{R_E}$ (Tsyganenko & Fairfield, 2004), which leaves flapping and warping as the main deforming factors during MMS magnetotail seasons.

To investigate the warping of the magnetotail plasma sheet, we consider the Earth's dipole tilt angle Ψ obtained from the MMS Magnetic Ephemerides Coordinates (MEC) dataset generated by Henderson et al. (2018). In GSM coordinates, Ψ, constrained in the X–Z plane, is the angle between the Earth's dipole tilt axis and the Z axis, which is positive when the Earth tilts toward the Sun and negative away from the Sun. Due to the daily Earth rotation, Ψ varies almost sinusoidally with an amplitude of about $10°$ and a period of about 1 day (not shown). Fig. 5 shows the distribution of Ψ with respect to (a) the time of year and (b) the concurrent MMS spacecraft position in Y.

In (a), there are two peaks separated by $\sim 20°$ due to the daily variation of Ψ and the seasonal variation of the dipole tilt (Ψ is lower in October). The daily variation is

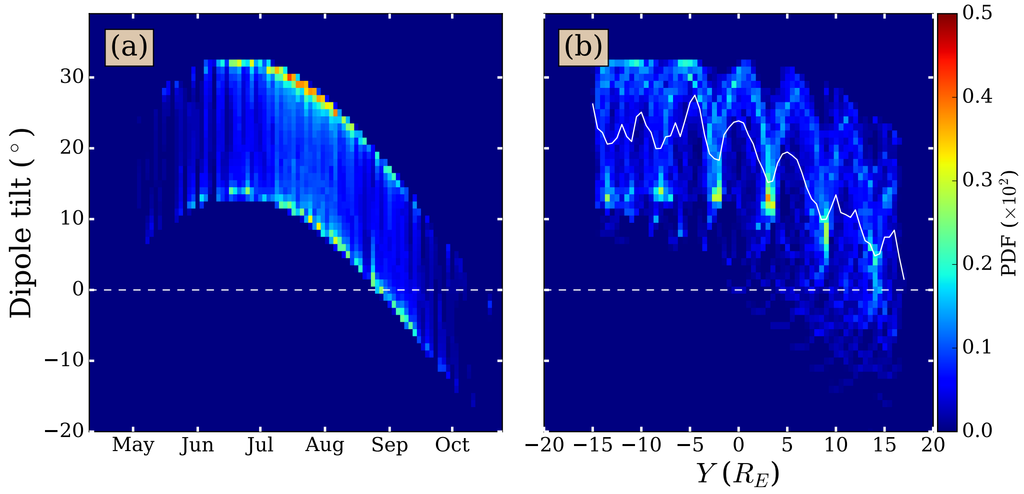

Figure 5. Distribution of the dipole tilt angle Ψ (a) in time and (b) in Y. The average Ψ is plotted as the solid white line in (b).

also seen in panel (b). However, (b) also shows that Ψ is lower at higher Y. The correlation between Ψ and Y is due to low natural precession of the MMS orbit, which causes MMS to visit the magnetotail only in the summer months. In these seasons, MMS enters the magnetotail from the dawn-side flank ($Y \sim -15\,\mathrm{R_E}$) around May when Ψ is high and exits to the dusk-side flank ($Y \sim 15\,\mathrm{R_E}$) around October when Ψ is low. The solid white line in (b) shows the average value of Ψ in terms of Y, which is around 20° in the dawn sector ($Y < 0$) and gradually decreases to zero in the dusk sector ($Y > 0$). The difference in average Ψ between these two sectors can lead to significant variations as a function of Y due to dipole tilt warping effects.

Using the same bin size as that in Fig. 2 ($0.5\,\mathrm{R_E}$), Fig. 6 shows the (Y averaged) spatial structure of (a) the ion plasma beta β_i, (b) the equatorial magnetic field B_{xy}, and (c) the normal electric field E_z. Similarly, Fig. 7 shows the (X averaged) spatial structure of (a) B_x and (b) Ψ. The structures of these parameters altogether provide a 3D picture of the plasma sheet, with the tilt angle Ψ indicating the degree of warping.

In Fig. 6 from (a) to (c), the bins are marked with a dot if they satisfy the beta condition, the magnetic field condition, and both (the plasma sheet condition in Table 1), respectively. The features in this figure correspond one-to-one with those discussed in Table 1. First, in Fig. 6(a), while constraining β_i to high values mostly excludes envi-

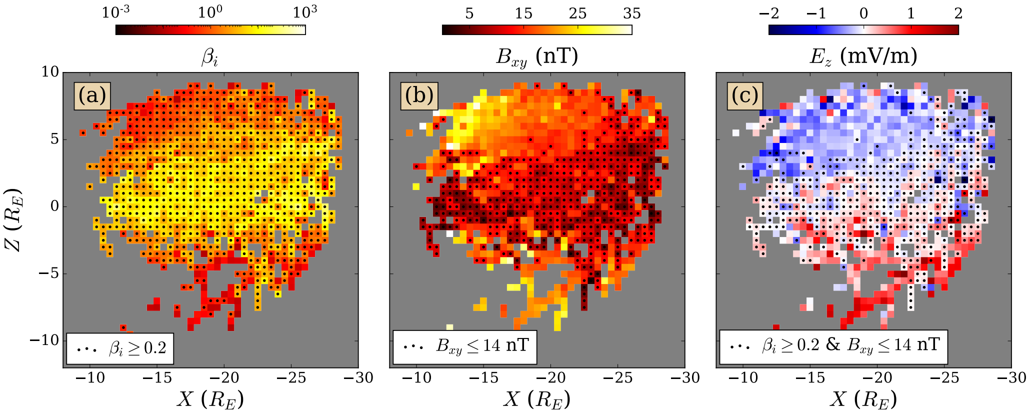

Figure 6. Spatial distribution in the X–Z plane of (a) β_i, (b) B_{xy}, and (c) E_z. In (a), marked bins (those with a circle marker at the center) satisfy the PS beta condition $\beta_i \geq 0.2$ in Table 1. Similarly, the marked bins satisfy the PS field condition $B_{xy} \leq 14\,\text{nT}$ in (b). Those in (c) satisfy both, the full PS condition.

ronments consistent with the lobe, the PSBL and PS can extend widely in Z. So the beta condition does not reveal much about the spatial extent. In Fig. 6(b), the magnetic field condition excludes the PSBL regions, leaving the remaining PS, which is more narrow along $Z = 0$. In Fig. 6(c), the normal electric field E_z that supports the cross-tail drift current $J_y \propto -E_z B_x$ also roughly follows this spatial structure. This electric field always points towards the inner PS (negative/positive in the northern/southern lobe) and tends to zero at the NS. This plot shows that the PS threshold condition agrees with the spatial structure of the PS, as drawn out by the normal electric field (E_z) and equatorial magnetic field (B_{xy}).

The spatial extent of E_z in the Z direction seemingly flares up to $\sim$ 8–10 $\mathrm{R_E}$ beyond $|X| \gtrsim 20\,\mathrm{R_E}$, while at closer distances, its structure is mainly located within $5\,\mathrm{R_E}$ of the equator. This flaring in the Z direction of the plasma sheet can be explained with variations in the Y direction caused by the dipole tilt. In Fig. 7(a), the two lobes are clearly distinguishable, with $B_x > 0$ indicating the northern hemisphere and $B_x < 0$ indicating the southern hemisphere. The null point $B_x \sim 0$ is the location of the neutral sheet. In (b), the distribution of Ψ also reflects the aforementioned dawn-dusk asymmetry in Fig. 5, where Ψ varies between 10° and 30° in the dawn sector ($Y < 0$) and between -10° and 10° in the dusk sector ($Y > 0$).

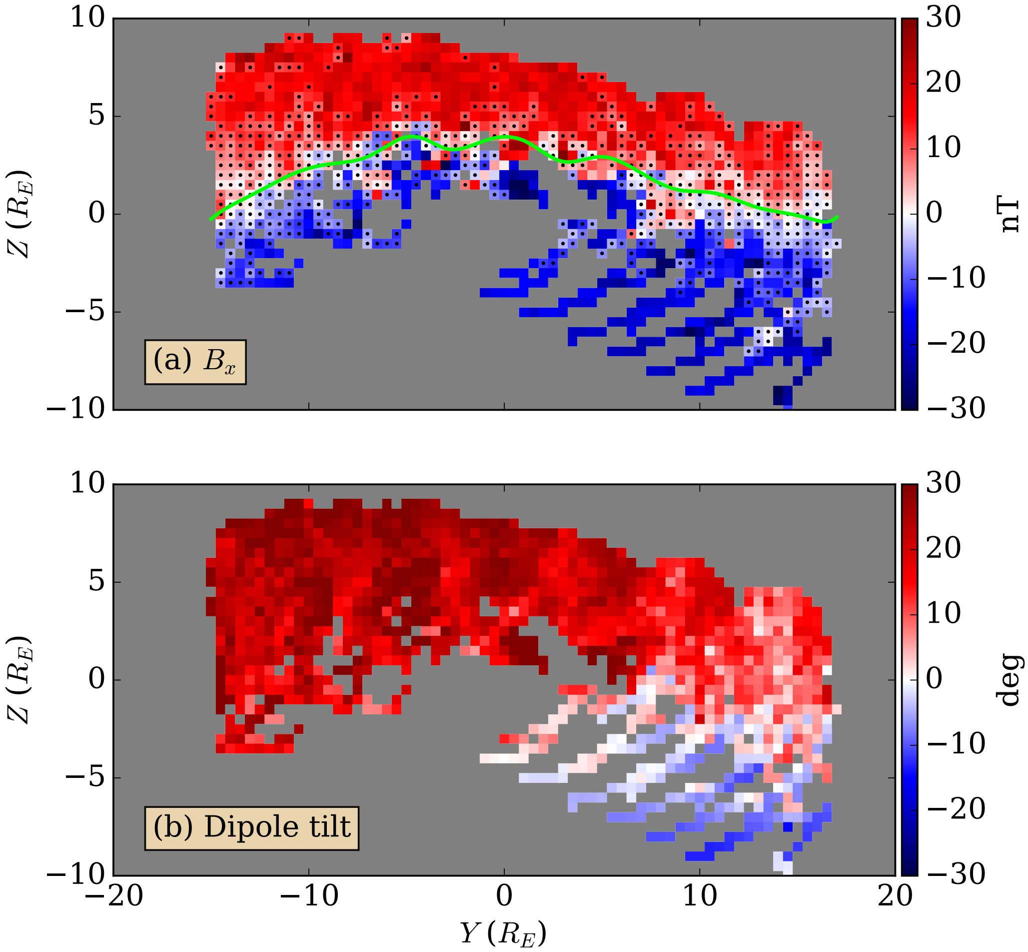

Figure 7. Spatial distribution in the Y–Z plane of (a) B_x and (b) the dipole tilt angle Ψ. The solid lime line in (a) is a global tail neutral sheet model (Xiao et al., 2016) dependent on Ψ and the average solar wind pressure $P_{\rm sw} = 2\,{\rm nPa}$. Similar to Fig. 6(c), the marked bins satisfy the plasma sheet condition (plotted in the same format).

Bins marked with a dot in Fig. 7(a) indicate the region satisfying the PS condition in Table 1. The reversal of B_x shows that the neutral sheet is located within the marked plasma sheet. The lime curve is a global NS model from Xiao et al. (2016), dependent on the dipole tilt angle and the solar wind pressure (see Appendix B). We use the average value of Ψ obtained from Fig. 5(b) (solid white line) for the former, and average OMNI observations $P_{\mathrm{sw}} = 2\,\mathrm{nPa}$ for the latter. The small variations in this model are highly dependent on those in Ψ, which in turn is affected by the spacecraft apogee. However, its average shows a remarkable agreement with the B_x reversal.

In Fig. 7(b), the high values of Ψ in the dawn sector causes the magnetotail to be warped to $\sim$ 2–4 $\mathrm{R_E}$ in Z, while in the dusk sector, there is little warping. The combination of warping in the dusk sector with no warping in the dawn sector contributes to the apparent flaring in X–Z seen in Fig. 6, as the Y direction is averaged in that figure. The plasma sheet extent around the neutral sheet in Fig. 7(a) seems to increase towards the flanks ($\sim$ 2–3 $\mathrm{R_E}$). This increase may be explained by kink-like flapping waves that are commonly observed in these regions (Gao et al., 2018). As the magnetic field condition is more strictly constrained to lower threshold, the outer PS is excluded and will result in a spatial distribution that follow the NS more closely.

6 Discussions and Conclusions

In summary, using a large volume of MMS data with combined plasma moments from the low-energy plasma and energetic particle instruments, we have investigated the background plasma conditions and the 3D spatial structure of the magnetotail plasma sheet using the threshold, imaging, and modeling approaches. Consequently, we have statistically distinguished inner-magnetotail environments corresponding to the plasma sheet, plasma sheet boundary layers, and lobes. We find that these methods are in good agreements, showing that the neutral sheet is embedded within a thick region of the plasma sheet, and they are both highly warped in the dawn sector and less deformed in the dusk sector.

This asymmetry is attributed to changes in the dipole tilt angle as the Earth orbits the Sun (see Figs. 5 and 7). But this observation is, in part, also specific to MMS, since the mission always visits the magnetotail in the summer months due to its orbital design. Fig. 8 provides a schematic of the Earth's magnetospheric configurations dur-

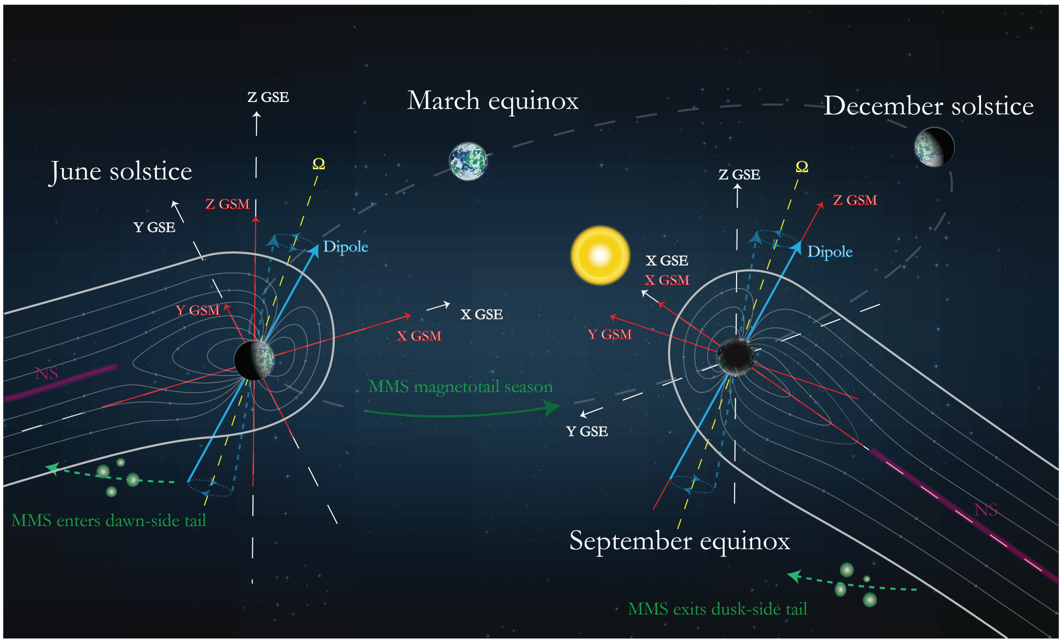

Figure 8. Schematic of Earth's magnetospheric configurations during an MMS magnetotail season. The Earth's rotational axis (Ω, dashed yellow) is constant. The magnetic dipole moment (solid blue arrow) rotates around this axis once a day, warping the magnetotail up and down in Z GSM. Around June solstice, MMS (green dots) enters the magnetotail from the dawn side. During this period, GSM (red) coincides with GSE (white) coordinates whenever the moment lies in the XZ plane. The tilt angle is large, resulting in a highly warped magnetotail in the positive Z direction. Towards September equinox, MMS exits the magnetotail from the dusk side. During this period, whenever the moment lies in the YZ plane, the Z axis of GSM coordinate is parallel with the dipole moment. The small tilt angle results in a relaxed magnetotail.

ing these periods. As MMS enters the magnetotail from the dawn-side flank around June solstice, the Earth's dipole on average tilts around 20° towards the Sun, resulting in a highly warped neutral sheet at $Z \sim 2$–$4\,\mathrm{R_E}$ [see Fig. 7(a)]. But when it exits the magnetotail from the dusk-side flank around September equinox, the average tilt angle is zero, leading to a less deformed and displaced neutral sheet.

While we have demonstrated that the deformation of the magnetotail mainly comes from warping, there remains flaring effects due to kink-like flapping waves or IMF twisting near the flanks that are not discussed in details in this paper. Future studies may need to consider smaller-scale evolution and utilize timing analysis to investigate properties of the flapping in further details. However, the insights about the plasma sheet spatial variations reported in this paper will be useful for future MMS magnetotail studies when considering its configuration and the state of the plasma sheet.

The threshold conditions in Fig. 3 and Table 1 are also in good agreement with a previous Cluster study (Boakes et al., 2014). The average current amplitude in the PS agrees with Cluster observations. However, lobe currents with amplitude comparable to those in the PS are also detected, albeit their occurrence rate is lower [Fig. 3(a–b), Fig. 4]. One interpretation of their presence is that thin electron-scale currents are resolved in the curlometer calculation due to MMS mission design with smaller average spacecraft separation in the magnetotail (Paschmann & Daly, 1998; Dunlop et al., 2021). While small-scale current systems have been observed with Cluster via the particle distribution function (Teste et al., 2007), its larger average separation inherently leads to underestimation of electron-scale currents via the curlometer technique. Finally, the ion plasma beta condition is slightly higher (by a factor of 2), probably due to the additional contribution of energetic (60–500 keV) ions to the total pressure. However, the threshold is still on the same order as that reported by B14, so our results are still consistent. Nevertheless, this might also be a demonstration that the combined plasma moments (discussed in Fig. 1) are important for studies of the magnetotail, especially those involving ion properties. While the difference in large statistical averages is small, that on a case-by-case basis might be significant. Finally, the region of interest (inner magnetotail) is more methodically defined, well-separated from solar wind data and mixed plasma regions near the flank-side boundary layers.

To perform the statistical analysis in this paper, we utilize around 316 continuous days of magnetotail observations by MMS (about 400 million field measurements and 6 million particle measurements), with data from a broad array of field and particle instruments. The dataset compiled in this study is useful not only for studying background plasma properties, but also for kinetic-scale dynamical evolution. Particularly, the intervals in our data contain continuous high-quality electric field measurements from EDP of at least 1 minute. Combined with accurate spatial gradient calculations, spectral analysis, and particle measurements, this enables future statistical studies of field fluctuations, particle energization, and their correlation. Further investigations of this data will reveal insights in the frequency of events such as the one in Fig. 1, and the properties and spatial variations of plasma turbulence and reconnection in the inner magnetotail.

Availability Statement

The MMS dataset, including ephemerides MEC data, is publicly available at the MMS Science Data Center (https://lasp.colorado.edu/mms/sdc/public/). Data are analyzed using the SPEDAS software package (http://spedas.org/blog/). All figures are generated with matplotlib, a Python visualization package (https://matplotlib.org/).

Acknowledgments

This work is supported by NASA's MMS (NNG04EB99C) mission. The authors thank the entire MMS team for their work on the mission. Specifically, they thank B. Mauk, B. Giles, and A. Narges for helpful conversations about the EPD, FPI, and EDP instruments and data products, S. Schwartz for suggesting the number-energy flux conversion table in the ISSI/ESA report, and P. Reiff for helpful comments on the sketch in Figure 8.

Appendix A FPI-FEEPS combined plasma moments

In this section, we describe the technical details pertaining to the combined FPI and FEEPS moment calculations. Since the data products for the distribution function from each instrument and their limitations are different, their combination is non-trivial. Every instrument is constrained within a certain energy range. So the derived plasma moments from the distribution function are only partial contributions. However, the main moments of interest for this study, the number density and scalar pressure, are additive scalars. So it is possible to sum the low- and high-energy contributions to get a total partial plasma moments. In the following, "low-energy" refers to the FPI measurements, while "high-energy" contains both the FEEPS measurements and the extrapolated energy-coverage gap between the two instruments.

At the low energy range, the FPI instrument provides a 3D distribution function $f(E, \varphi, \theta)$ in spherical coordinates with the energy $E = (1/2)mv^2$ measured at 32 different channels from 6.32 eV to 27.5 keV for electrons and from 2.16 eV to 28.3 keV for ions (Pollock et al., 2016). m is the mass of the particle species. Averaged over a solid angle $d\Omega = d(\cos\theta)d\varphi$, the differential energy flux, defined as (Larsen et al., 2022)

Table A1. Periods of lobe observations used for background estimation.

	Start	Stop
1	2017-07-04/04:50	2017-07-04/05:20
2	2017-07-07/02:30	2017-07-07/03:20
3	2017-07-10/07:20	2017-07-10/09:20
4	2017-07-13/09:30	2017-07-13/10:10
5	2017-07-15/15:20	2017-07-15/16:40

$$\frac{d\mathcal{F}}{dE} = \frac{v^4}{2} \frac{\int d\Omega f(E, \varphi, \theta)}{\int d\Omega}, \tag{A1}$$

is solely a function of energy, provided in the FPI data products as an energy-angle spectrogram. While FPI also provides partial moments calculated from the full 3D distribution function (which undergoes multiple conditioning and processing steps by default for integration such as spin-tone correction, penetrating radiation removal, etc, while the energy flux does not), those moments are not reliable when there is significant cold ($\sim$ 10-100 eV) plasma contribution. In particular, the ion energy flux can be contaminated with background radiation (energetic electrons) up to keV energies, and the electron distribution is often contaminated with photoelectrons due to spacecraft charging effects (up to $\sim$ 100 eV). Thus, as a rule of thumb, caution to the plasma moments is needed when the density is below $0.05\,\mathrm{cm}^3$.

To push the limits of FPI in our combined moments calculation, we apply the usual processing steps to the omni-directional energy flux with an addition of a background removal. Fig. A1 shows the average energy fluxes of ions and electrons during 5 nominally quiet lobe periods in July 2017 (selected by eyes, see Table A1). In (a), the ion distribution shows two constant background populations for the FPI and FEEPS energy ranges, respectively. In (b), there are a cold photoelectron background up to about 1 keV, and a variable population throughout the remaining FPI range. In our dataset, we remove these populations using the displayed step functions (solid black). The resulting omni-directional energy flux is used in conjunction with FEEPS data to calculate a combined spectrum, as shown in Fig. 1(d–e).

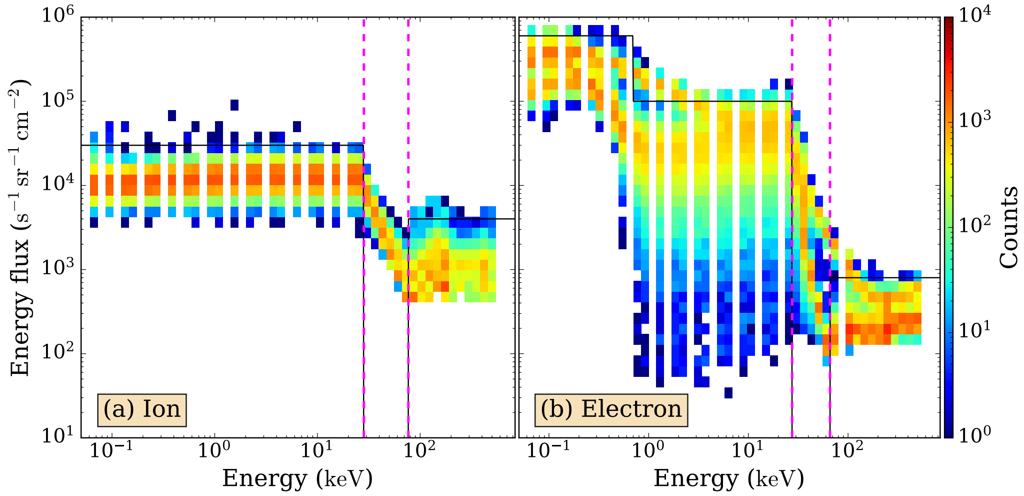

Figure A1. Average values of the (a) ion and (b) electron energy fluxes during nominal lobe periods. The step functions (in black) are used to remove background populations in the data used in this study.

At the high energy range, the FEEPS instrument provides a coarse instantaneous all-sky view of electrons and ions, whose angular coverage can be refined by means of rotation (Blake et al., 2016; Mauk et al., 2016). While the design of the field-of-view is different for each particle species, the all-sky measurements can be combined into an omni-directional number flux spectrogram, which is related to the energy flux (see Table D.2 of Wüest et al., 2007) by

$$\frac{d\mathcal{N}}{dE} = \frac{1}{E}\frac{d\mathcal{F}}{dE}, \tag{A2}$$

with E measured from 33.2 keV to 509.2 keV for electrons and from 57.9 keV to 558.6 keV for ions. The lowest-energy channel in FEEPS is excluded due to noise. In Fig. 1(d–e), the FEEPS number flux has been converted to energy flux with Eq. (A2) in the combined spectrogram. Five data points are linearly extrapolated to cover the energy gap between the two instruments. While a linear extrapolation might not be adequate to estimate the missing data in the gap, we note that this method of extrapolation does not add false data and only underestimate the contribution of missing data in the gap.

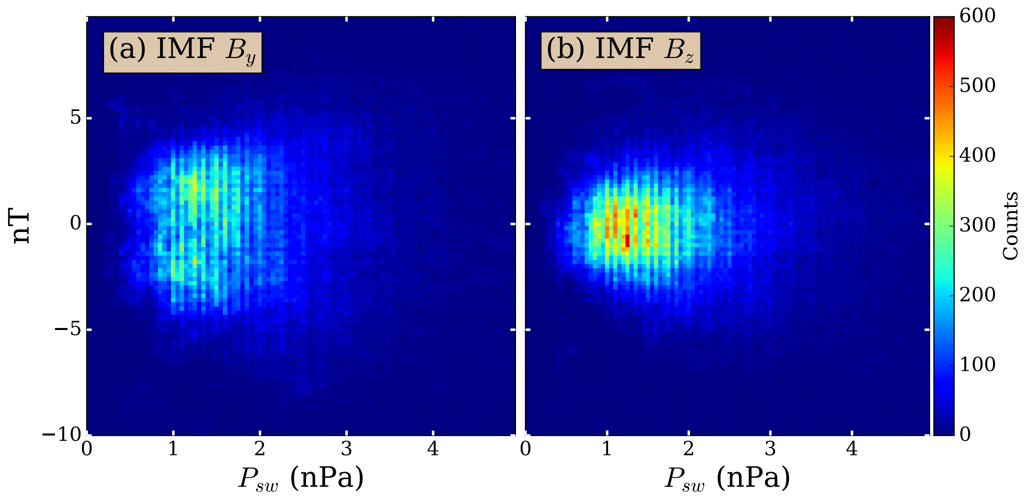

Figure B1. Distribution of (a) the IMF B_y and (b) the IMF B_z with respect to total (dynamical and magnetic) solar wind pressure during MMS magnetotail observations.

It is reasonable to assume that the bulk flow rarely surpasses the FPI energy range. Therefore, the omni-directional, high-energy contribution to the partial number density and scalar pressure can be integrated as (see also Mauk et al., 2004)

$$n_{\mathrm{hi}} = 4\pi\sqrt{\frac{m}{2}} \int \left(\sqrt{E}dE\right)\left(\frac{1}{E}\frac{d\mathcal{N}}{dE}\right), \qquad \text{and} \qquad P_{\mathrm{hi}} = 4\pi\sqrt{\frac{m}{2}} \int \left(\sqrt{E}dE\right)\frac{d\mathcal{N}}{dE}, \tag{A3}$$

where $\sqrt{E}dE \sim v^2 dv$ and from Eqs. (A1) and (A2), $(1/E)d\mathcal{N}/dE \sim f$. The energy range in above integrals covers both the extrapolated range and FEEPS range. Finally, the total number density and scalar pressure, shown in Fig. 1(f–g), are $n_{\mathrm{total}} = n_{\mathrm{lo}} + n_{\mathrm{hi}}$ and $P_{\mathrm{total}} = P_{\mathrm{lo}} + P_{\mathrm{hi}}$. Potentially, these considerations can also be extended to other quantities such as the isotropic parts of the temperature and the heat flux. In general, the resulting ion and electron densities calculated with the steps as laid out above preserve charge quasi-neutrality very well, even during periods of low FPI density (see Fig. 1f), which provides confidence in the statistical analyses discussed in the main text.

Appendix B Solar wind and IMF conditions during MMS magnetotail observations and global magnetospheric models

The OMNI dataset (King & Papitashvili, 2005) provides 1-minute averaged solar wind and interplanetary magnetic field (IMF) conditions. From this dataset, we plot in

Fig. B1 the distribution of (a) the IMF B_y and (b) the IMF B_z with respect to the total solar wind pressure (including magnetic field pressure and dynamical pressure) during the magnetotail seasons constrained by the criteria in Section 3. Different from the counting statistics discussed in the main text, each count here represents a 1-min observation. From this figure, B_y averages around 1–2 nT, while B_z averages around zero. The total solar wind pressure averages around 1–2 nPa, with the most extreme pressure around 4–5 nPa.

In this study, two global magnetospheric models are utilized for our analysis of MMS observations. Lin et al. (2010) used a database of magnetopause crossings (observed from 1994 to 2008) from Cluster, Geotail, GOES, IMP 8, Interball, LANL, Polar, TC1, and THEMIS, together with solar wind conditions from ACE and Wind to construct an asymmetric 3D magnetopause model in aberrated GSM coordinates. This model (see Equations (19–20) in their paper) depends on the IMF B_z, the total solar wind pressure, and the Earth's dipole tilt angle Ψ. since the average Ψ changes between the dawn and dusk sectors [see Figs. 5 and 7], we set $\Psi = 0$ and use average values in Fig. B1(b) for the magnetopause shapes in Fig. 2(b–d). The models also need to be tilted 5° clockwise to better fit the changes in background plasma conditions between the solar wind and inner magnetotail. This rotation is needed due to either the seasonal variations of Ψ, or the usage of GSM coordinates throughout the paper.

Xiao et al. (2016) used magnetic field data from Cluster, Geotail, TC-1, and THEMIS from 1995 to 2013 to fit the average shape and position of the magnetotail neutral sheet. Their model (see Equations (4–7) in their paper) is consistent with that in Tsyganenko and Fairfield (2004) and depends on the Y coordinate, the Earth's dipole tilt angle Ψ, and scaling parameters normalized for a downtail distance of 20,$\mathrm{R_E}$ and solar wind pressure of 2 nPa. This pressure is typical from OMNI observations in Fig. B1. We use the average value of Ψ in terms of Y from Fig. 5(b) so that this NS model, as shown in Fig. 7(a), is only dependent on the Y coordinate. In our analysis, we have also found little variations of the results for different X downtail distance, so the scaling parameters normalized for $X = -20\,\mathrm{R_E}$ are reasonable.

References

Amit, H., & Olson, P. (2008, feb). Geomagnetic dipole tilt changes induced by core flow. *Physics of the Earth and Planetary Interiors*, *166*(3-4), 226–238. Retrieved from https://linkinghub.elsevier.com/retrieve/pii/S0031920108000253 doi: 10.1016/j.pepi.2008.01.007

Angelopoulos, V., Kennel, C. F., Coroniti, F. V., Pellat, R., Kivelson, M. G., Walker, R. J., … Gosling, J. T. (1994). Statistical characteristics of bursty bulk flow events. *Journal of Geophysical Research*, *99*(A11), 21257. Retrieved from http://doi.wiley.com/10.1029/94JA01263 doi: 10.1029/94JA01263

Angelopoulos, V., Sibeck, D., Carlson, C. W., McFadden, J. P., Larson, D., Lin, R. P., … Sigwarth, J. (2008, dec). First Results from the THEMIS Mission. *Space Science Reviews*, *141*(1-4), 453–476. Retrieved from http://link.springer.com/10.1007/s11214-008-9378-4 doi: 10.1007/s11214-008-9378-4

Artemyev, A., Lu, S., El-Alaoui, M., Lin, Y., Angelopoulos, V., Zhang, X., … Russell, C. (2021, mar). Configuration of the Earth's Magnetotail Current Sheet. *Geophysical Research Letters*, *48*(6), 1–9. Retrieved from https://onlinelibrary.wiley.com/doi/10.1029/2020GL092153 doi: 10.1029/2020GL092153

Åsnes, A., Friedel, R. W. H., Lavraud, B., Reeves, G. D., Taylor, M. G. G. T., & Daly, P. (2008, mar). Statistical properties of tail plasma sheet electrons above 40 keV. *Journal of Geophysical Research: Space Physics*, *113*(A3), n/a–n/a. Retrieved from http://doi.wiley.com/10.1029/2007JA012502 doi: 10.1029/2007JA012502

Baumjohann, W., Paschmann, G., & Cattell, C. A. (1989, jun). Average plasma properties in the central plasma sheet. *Journal of Geophysical Research: Space Physics*, *94*(A6), 6597–6606. Retrieved from http://doi.wiley.com/10.1029/JA094iA06p06597 doi: 10.1029/JA094iA06p06597

Baumjohann, W., Paschmann, G., Sckopke, N., Cattell, C. A., & Carlson, C. W. (1988). Average ion moments in the plasma sheet boundary layer. *Journal of Geophysical Research*, *93*(A10), 11507. Retrieved from http://doi.wiley.com/10.1029/JA093iA10p11507 doi: 10.1029/JA093iA10p11507

Blake, J. B., Mauk, B. H., Baker, D. N., Carranza, P., Clemmons, J. H., Craft, J. V., … Westlake, J. (2016, mar). The Fly's Eye Energetic Particle Spectrometer (FEEPS) Sensors for the Magnetospheric Multiscale

(MMS) Mission. *Space Science Reviews*, *199*(1-4), 309–329. Retrieved from http://link.springer.com/10.1007/s11214-015-0163-x doi: 10.1007/s11214-015-0163-x

Boakes, P. D., Nakamura, R., Volwerk, M., & Milan, S. E. (2014, aug). ECLAT Cluster Spacecraft Magnetotail Plasma Region Identifications (2001–2009). *Dataset Papers in Science*, *2014*, 1–13. Retrieved from https://www.hindawi.com/journals/dpis/2014/684305/ doi: 10.1155/2014/684305

Burch, J., Moore, T. E., Torbert, R. B., & Giles, B. L. (2016, mar). Magnetospheric Multiscale Overview and Science Objectives. *Space Science Reviews*, *199*(1-4), 5–21. Retrieved from http://link.springer.com/10.1007/s11214-015-0164-9 doi: 10.1007/s11214-015-0164-9

Cattell, C. A., Mozer, F. S., Hones, E. W., Anderson, R. R., & Sharp, R. D. (1986). ISEE observations of the plasma sheet boundary, plasma sheet, and neutral sheet: 1. Electric field, magnetic field, plasma, and ion composition. *Journal of Geophysical Research*, *91*(A5), 5663. Retrieved from http://doi.wiley.com/10.1029/JA091iA05p05663 doi: 10.1029/JA091iA05p05663

Chasapis, A., Yang, Y., Matthaeus, W. H., Parashar, T. N., Haggerty, C. C., Burch, J., … Russell, C. T. (2018, jul). Energy Conversion and Collisionless Plasma Dissipation Channels in the Turbulent Magnetosheath Observed by the Magnetospheric Multiscale Mission. *The Astrophysical Journal*, *862*(1), 32. Retrieved from https://iopscience.iop.org/article/10.3847/1538-4357/aac775 doi: 10.3847/1538-4357/aac775

Chen, L., Wang, S., Hesse, M., Ergun, R. E., Moore, T., Giles, B., … Lindqvist, P. (2019, jun). Electron Diffusion Regions in Magnetotail Reconnection Under Varying Guide Fields. *Geophysical Research Letters*, *46*(12), 6230–6238. Retrieved from https://onlinelibrary.wiley.com/doi/10.1029/2019GL082393 doi: 10.1029/2019GL082393

Chong, G. S., Pitkänen, T., Hamrin, M., & Kullen, A. (2022, apr). Dawn-Dusk Ion Flow Asymmetry in the Plasma Sheet: Interplanetary Magnetic Field B y Versus Distance With Respect to the Neutral Sheet. *Journal of Geophysical Research: Space Physics*, *127*(4). Retrieved from https://onlinelibrary.wiley.com/doi/10.1029/2021JA030208 doi: 10.1029/2021JA030208

Coroniti, F. V., & Kennel, C. F. (1972, jul). Changes in magnetospheric configuration during the substorm growth phase. *Journal of Geophysical Research*, *77*(19), 3361–3370. Retrieved from http://doi.wiley.com/10.1029/JA077i019p03361 doi: 10.1029/JA077i019p03361

Cowley, S. (1991, jul). The structure and length of tail-associated phenomena in the solar wind downstream from the Earth. *Planetary and Space Science*, *39*(7), 1039–1043. Retrieved from https://linkinghub.elsevier.com/retrieve/pii/003206339190110V doi: 10.1016/0032-0633(91)90110-V

Coxon, J. C., Jackman, C. M., Freeman, M. P., Forsyth, C., & Rae, I. J. (2016, feb). Identifying the magnetotail lobes with Cluster magnetometer data. *Journal of Geophysical Research: Space Physics*, *121*(2), 1436–1446. Retrieved from https://onlinelibrary.wiley.com/doi/abs/10.1002/2015JA022020 doi: 10.1002/2015JA022020

Dayeh, M. A., Fuselier, S. A., Funsten, H. O., McComas, D. J., Ogasawara, K., Petrinec, S. M., … Valek, P. (2015, apr). Shape of the terrestrial plasma sheet in the near-Earth magnetospheric tail as imaged by the Interstellar Boundary Explorer. *Geophysical Research Letters*, *42*(7), 2115–2122. Retrieved from http://doi.wiley.com/10.1002/2015GL063682 doi: 10.1002/2015GL063682

Dungey, J. W. (1965, apr). The length of the magnetospheric tail. *Journal of Geophysical Research*, *70*(7), 1753–1753. Retrieved from http://doi.wiley.com/10.1029/JZ070i007p01753 doi: 10.1029/JZ070i007p01753

Dunlop, M. W., Dong, X., Wang, T., Eastwood, J. P., Robert, P., Haaland, S., … De Keyser, J. (2021, nov). Curlometer Technique and Applications. *Journal of Geophysical Research: Space Physics*, *126*(11). Retrieved from https://onlinelibrary.wiley.com/doi/10.1029/2021JA029538 doi: 10.1029/2021JA029538

Eastman, T. E., Frank, L. A., Peterson, W. K., & Lennartsson, W. (1984). The plasma sheet boundary layer. *Journal of Geophysical Research*, *89*(A3), 1553. Retrieved from http://doi.wiley.com/10.1029/JA089iA03p01553 doi: 10.1029/JA089iA03p01553

Ergun, R. E., Ahmadi, N., Kromyda, L., Schwartz, S. J., Chasapis, A., Hoilijoki, S., … Giles, B. L. (2020a, aug). Observations of Particle Acceleration in Magnetic

Reconnection–driven Turbulence. *The Astrophysical Journal*, *898*(2), 154. Retrieved from https://iopscience.iop.org/article/10.3847/1538-4357/ab9ab6 doi: 10.3847/1538-4357/ab9ab6

Ergun, R. E., Ahmadi, N., Kromyda, L., Schwartz, S. J., Chasapis, A., Hoilijoki, S., … Burch, J. (2020b, aug). Particle Acceleration in Strong Turbulence in the Earth's Magnetotail. *The Astrophysical Journal*, *898*(2), 153. Retrieved from https://iopscience.iop.org/article/10.3847/1538-4357/ab9ab5 doi: 10.3847/1538-4357/ab9ab5

Ergun, R. E., Andersson, L., Tao, J., Angelopoulos, V., Bonnell, J. W., McFadden, J. P., … Baumjohann, W. (2009, apr). Observations of Double Layers in Earth's Plasma Sheet. *Physical Review Letters*, *102*(15), 155002. Retrieved from https://link.aps.org/doi/10.1103/PhysRevLett.102.155002 doi: 10.1103/PhysRevLett.102.155002

Ergun, R. E., Goodrich, K. A., Stawarz, J. E., Andersson, L., & Angelopoulos, V. (2015, mar). Large-amplitude electric fields associated with bursty bulk flow braking in the Earth's plasma sheet. *Journal of Geophysical Research: Space Physics*, *120*(3), 1832–1844. Retrieved from https://onlinelibrary.wiley.com/doi/10.1002/2014JA020165 doi: 10.1002/2014JA020165

Ergun, R. E., Goodrich, K. A., Wilder, F. D., Ahmadi, N., Holmes, J. C., Eriksson, S., … Vaivads, A. (2018, apr). Magnetic Reconnection, Turbulence, and Particle Acceleration: Observations in the Earth's Magnetotail. *Geophysical Research Letters*, *45*(8), 3338–3347. Retrieved from https://onlinelibrary.wiley.com/doi/abs/10.1002/2018GL076993 doi: 10.1002/2018GL076993

Ergun, R. E., Tucker, S., Westfall, J., Goodrich, K. A., Malaspina, D. M., Summers, D., … Cully, C. M. (2016, mar). The Axial Double Probe and Fields Signal Processing for the MMS Mission. *Space Science Reviews*, *199*(1-4), 167–188. Retrieved from http://link.springer.com/10.1007/s11214-014-0115-x doi: 10.1007/s11214-014-0115-x

Ergun, R. E., Usanova, M. E., Turner, D. L., & Stawarz, J. E. (2022, jun). Bursty Bulk Flow Turbulence as a Source of Energetic Particles to the Outer Radiation Belt. *Geophysical Research Letters*, *49*(11). Retrieved from https://onlinelibrary.wiley.com/doi/10.1029/2022GL098113 doi: 10.1029/2022GL098113

Escoubet, C. P., Fehringer, M., & Goldstein, M. (2001, sep). The Cluster mission: Introduction. *Annales Geophysicae*, *19*(10/12), 1197–1200. Retrieved from https://angeo.copernicus.org/articles/19/1197/2001/ doi: 10.5194/angeo-19-1197-2001

Fairfield, D. H., Otto, A., Mukai, T., Kokubun, S., Lepping, R. P., Steinberg, J. T., … Yamamoto, T. (2000, sep). Geotail observations of the Kelvin-Helmholtz instability at the equatorial magnetotail boundary for parallel northward fields. *Journal of Geophysical Research: Space Physics*, *105*(A9), 21159–21173. Retrieved from http://doi.wiley.com/10.1029/1999JA000316 doi: 10.1029/1999JA000316

Fuselier, S. A., Lewis, W. S., Schiff, C., Ergun, R., Burch, J., Petrinec, S. M., & Trattner, K. J. (2016, mar). Magnetospheric Multiscale Science Mission Profile and Operations. *Space Science Reviews*, *199*(1-4), 77–103. Retrieved from https://link.springer.com/10.1007/s11214-014-0087-x doi: 10.1007/s11214-014-0087-x

Gao, J. W., Rong, Z. J., Cai, Y. H., Lui, A. T. Y., Petrukovich, A. A., Shen, C., … Wan, W. X. (2018, sep). The Distribution of Two Flapping Types of Magnetotail Current Sheet: Implication for the Flapping Mechanism. *Journal of Geophysical Research: Space Physics*, *123*(9), 7413–7423. Retrieved from http://doi.wiley.com/10.1029/2018JA025695 doi: 10.1029/2018JA025695

Grigorenko, E. E., Koleva, R., & Sauvaud, J.-A. (2012, sep). On the problem of Plasma Sheet Boundary Layer identification from plasma moments in Earth's magnetotail. *Annales Geophysicae*, *30*(9), 1331–1343. Retrieved from https://angeo.copernicus.org/articles/30/1331/2012/ doi: 10.5194/angeo-30-1331-2012

Haaland, S., Kronberg, E. A., Daly, P. W., Fränz, M., Degener, L., Georgescu, E., & Dandouras, I. (2010, aug). Spectral characteristics of protons in the Earth's plasmasheet: statistical results from Cluster CIS and RAPID. *Annales Geophysicae*, *28*(8), 1483–1498. Retrieved from https://angeo.copernicus.org/articles/28/1483/2010/ doi: 10.5194/angeo-28-1483-2010

Hammond, C. M., Kivelson, M. G., & Walker, R. J. (1994). Imaging the effect of dipole tilt on magnetotail boundaries. *Journal of Geophysical Research*, *99*(A4), 6079. Retrieved from http://doi.wiley.com/10.1029/93JA01924 doi: 10.1029/93JA01924

Henderson, M., Morley, S., Niehof, J., & Larsen, B. A. (2018). *LANLGeoMag.* Zenodo. Retrieved from https://doi.org/10.5281/zenodo.1195041 doi: 10.5281/zenodo.1195041

Hietala, H., Drake, J. F., Phan, T. D., Eastwood, J. P., & McFadden, J. P. (2015, sep). Ion temperature anisotropy across a magnetotail reconnection jet. *Geophysical Research Letters*, *42*(18), 7239–7247. Retrieved from https://onlinelibrary.wiley.com/doi/10.1002/2015GL065168 doi: 10.1002/2015GL065168

Huang, S. Y., Wei, Y. Y., Yuan, Z. G., Jiang, K., Deng, X. H., Xu, S. B., … Zhang, Z. H. (2020). Electron Jets in the Terrestrial Magnetotail: A Statistical Overview. *The Astrophysical Journal*, *896*(1), 67. doi: 10.3847/1538-4357/ab8eb0

Johnson, J. R., Wing, S., & Delamere, P. A. (2014, nov). Kelvin Helmholtz Instability in Planetary Magnetospheres. *Space Science Reviews*, *184*(1-4), 1–31. Retrieved from http://link.springer.com/10.1007/s11214-014-0085-z doi: 10.1007/s11214-014-0085-z

King, J. H., & Papitashvili, N. E. (2005). Solar wind spatial scales in and comparisons of hourly Wind and ACE plasma and magnetic field data. *Journal of Geophysical Research*, *110*(A2), A02104. Retrieved from http://doi.wiley.com/10.1029/2004JA010649 doi: 10.1029/2004JA010649

Larsen, K., Burch, J., Giles, B., Clapsadle, J., Fowler, G., Torbert, R., … Pankratz, C. (2022). *Magnetospheric Multiscale (MMS) Project - Calibration and Measurement Algorithms Document (CMAD)* (Tech. Rep. No. October). Retrieved from https://lasp.colorado.edu/mms/sdc/public/

Lin, R. L., Zhang, X. X., Liu, S. Q., Wang, Y. L., & Gong, J. C. (2010, apr). A three-dimensional asymmetric magnetopause model. *Journal of Geophysical Research: Space Physics*, *115*(A4). Retrieved from http://doi.wiley.com/10.1029/2009JA014235 doi: 10.1029/2009JA014235

Liu, Y., Birn, J., Daughton, W., Hesse, M., & Schindler, K. (2014, dec). On-set of reconnection in the near magnetotail: PIC simulations. *Journal of Geophysical Research: Space Physics*, *119*(12), 9773–9789. Retrieved from `https://onlinelibrary.wiley.com/doi/10.1002/2014JA020492` doi: 10.1002/2014JA020492

Lui, A. T. Y., Meng, C.-I., & Akasofu, S.-I. (1978, apr). Wavy nature of the magnetotail neutral sheet. *Geophysical Research Letters*, *5*(4), 279–282. Retrieved from `http://doi.wiley.com/10.1029/GL005i004p00279` doi: 10.1029/GL005i004p00279

Malaspina, D. M., Wygant, J. R., Ergun, R. E., Reeves, G. D., Skoug, R. M., & Larsen, B. A. (2015, jun). Electric field structures and waves at plasma boundaries in the inner magnetosphere. *Journal of Geophysical Research: Space Physics*, *120*(6), 4246–4263. Retrieved from `https://onlinelibrary.wiley.com/doi/10.1002/2015JA021137` doi: 10.1002/2015JA021137

Mauk, B. H., Blake, J. B., Baker, D. N., Clemmons, J. H., Reeves, G. D., Spence, H. E., … Westlake, J. H. (2016, mar). The Energetic Particle Detector (EPD) Investigation and the Energetic Ion Spectrometer (EIS) for the Magnetospheric Multiscale (MMS) Mission. *Space Science Reviews*, *199*(1-4), 471–514. Retrieved from `http://link.springer.com/10.1007/s11214-014-0055-5` doi: 10.1007/s11214-014-0055-5

Mauk, B. H., Mitchell, D. G., McEntire, R. W., Paranicas, C. P., Roelof, E. C., Williams, D. J., & Krimigis, S. M. (2004). Energetic ion characteristics and neutral gas interactions in Jupiter's magnetosphere. *Journal of Geophysical Research*, *109*(A9), A09S12. Retrieved from `http://doi.wiley.com/10.1029/2003JA010270` doi: 10.1029/2003JA010270

McComas, D. J., Russell, C. T., Elphic, R. C., & Bame, S. J. (1986). The near-Earth cross-tail current sheet: Detailed ISEE 1 and 2 case studies. *Journal of Geophysical Research*, *91*(A4), 4287. Retrieved from `http://doi.wiley.com/10.1029/JA091iA04p04287` doi: 10.1029/JA091iA04p04287

Nakamura, R., Baumjohann, W., Nagai, T., Fujimoto, M., Mukai, T., Klecker, B., … Bogdanova, Y. (2004). Flow shear near the boundary of the plasma sheet observed by Cluster and Geotail. *Journal of Geophysical Research*, *109*(A5), A05204. Retrieved from `http://doi.wiley.com/10.1029/2003JA010174` doi: 10.1029/2003JA010174

Nykyri, K., Otto, A., Lavraud, B., Mouikis, C., Kistler, L. M., Balogh, A., & Rème, H. (2006, oct). Cluster observations of reconnection due to the Kelvin-Helmholtz instability at the dawnside magnetospheric flank. *Annales Geophysicae*, *24*(10), 2619–2643. Retrieved from `https://angeo.copernicus.org/articles/24/2619/2006/` doi: 10.5194/angeo-24-2619-2006

Otto, A., & Fairfield, D. H. (2000, sep). Kelvin-Helmholtz instability at the magnetotail boundary: MHD simulation and comparison with Geotail observations. *Journal of Geophysical Research: Space Physics*, *105*(A9), 21175–21190. Retrieved from `http://doi.wiley.com/10.1029/1999JA000312` doi: 10.1029/1999JA000312

Owen, C. J., Slavin, J. A., Richardson, I. G., Murphy, N., & Hynds, R. J. (1995). Average motion, structure and orientation of the distant magnetotail determined from remote sensing of the edge of the plasma sheet boundary layer with E > 35 keV ions. *Journal of Geophysical Research*, *100*(A1), 185. Retrieved from `http://doi.wiley.com/10.1029/94JA02417` doi: 10.1029/94JA02417

Paschmann, G., & Daly, P. (1998). *Analysis Methods for Multi-Spacecraft Data.*

Pedersen, A., Cattell, C. A., Fälthammar, C.-G., Knott, K., Lindqvist, P.-A., Manka, R. H., & Mozer, F. S. (1985). Electric fields in the plasma sheet and plasma sheet boundary layer. *Journal of Geophysical Research*, *90*(A2), 1231. Retrieved from `http://doi.wiley.com/10.1029/JA090iA02p01231` doi: 10.1029/JA090iA02p01231

Pollock, C., Moore, T., Jacques, A., Burch, J., Gliese, U., Saito, Y., … Zeuch, M. (2016, mar). Fast Plasma Investigation for Magnetospheric Multiscale. *Space Science Reviews*, *199*(1-4), 331–406. Retrieved from `http://link.springer.com/10.1007/s11214-016-0245-4` doi: 10.1007/s11214-016-0245-4

Rong, Z. J., Cai, Y. H., Gao, J. W., Lui, A. T. Y., Shen, C., Petrukovich, A. A., … Wan, W. X. (2018, jul). Cluster Observations of a Dispersive Flapping Event of Magnetotail Current Sheet. *Journal of Geophysical Research: Space Physics*, *123*(7), 5571–5579. Retrieved from `http://doi.wiley.com/10.1029/2018JA025196` doi: 10.1029/2018JA025196

Runov, A., Angelopoulos, V., Sergeev, V. A., Glassmeier, K.-H., Auster, U., McFadden, J., … Mann, I. (2009, jan). Global properties of magnetotail current sheet flapping: THEMIS perspectives. *Annales Geophysicae*, *27*(1), 319–328. Retrieved from https://angeo.copernicus.org/articles/27/319/2009/ doi: 10.5194/angeo-27-319-2009

Runov, A., Sergeev, V. A., Baumjohann, W., Nakamura, R., Apatenkov, S., Asano, Y., … Rème, H. (2005, jun). Electric current and magnetic field geometry in flapping magnetotail current sheets. *Annales Geophysicae*, *23*(4), 1391–1403. Retrieved from https://angeo.copernicus.org/articles/23/1391/2005/ doi: 10.5194/angeo-23-1391-2005

Russell, C. T., Anderson, B. J., Baumjohann, W., Bromund, K. R., Dearborn, D., Fischer, D., … Richter, I. (2016, mar). The Magnetospheric Multiscale Magnetometers. *Space Science Reviews*, *199*(1-4), 189–256. Retrieved from http://link.springer.com/10.1007/s11214-014-0057-3 doi: 10.1007/s11214-014-0057-3

Russell, C. T., & McPherron, R. L. (1973). The magnetotail and substorms. *Space Science Reviews*, *15*(2-3), 205–266. Retrieved from http://link.springer.com/10.1007/BF00169321 doi: 10.1007/BF00169321

Sanny, J., McPherron, R. L., Russell, C. T., Baker, D. N., Pulkkinen, T. I., & Nishida, A. (1994). Growth-phase thinning of the near-Earth current sheet during the CDAW 6 substorm. *Journal of Geophysical Research*, *99*(A4), 5805. Retrieved from http://doi.wiley.com/10.1029/93JA03235 doi: 10.1029/93JA03235

Sergeev, V., Runov, A., Baumjohann, W., Nakamura, R., Zhang, T. L., Volwerk, M., … Klecker, B. (2003, mar). Current sheet flapping motion and structure observed by Cluster. *Geophysical Research Letters*, *30*(6), 2–5. Retrieved from http://doi.wiley.com/10.1029/2002GL016500 doi: 10.1029/2002GL016500

Shukhtina, M. A., Dmitrieva, N. P., & Sergeev, V. A. (2004, mar). Quantitative magnetotail characteristics of different magnetospheric states. *Annales Geophysicae*, *22*(3), 1019–1032. Retrieved from https://angeo.copernicus.org/articles/22/1019/2004/ doi: 10.5194/angeo-22-1019-2004

Shustov, P. I., Zhang, X., Pritchett, P. L., Artemyev, A., Angelopoulos, V., Yushkov, E. V., & Petrukovich, A. A. (2019, jan). Statistical Properties of Sub-Ion Magnetic Holes in the Dipolarized Magnetotail: Formation, Structure, and Dynamics. *Journal of Geophysical Research: Space Physics*, *124*(1), 342–359. Retrieved from https://onlinelibrary.wiley.com/doi/10.1029/2018JA025852 doi: 10.1029/2018JA025852

Sitnov, M., Birn, J., Ferdousi, B., Gordeev, E., Khotyaintsev, Y., Merkin, V., … Zhou, X. (2019, jun). Explosive Magnetotail Activity. *Space Science Reviews*, *215*(4), 31. Retrieved from http://link.springer.com/10.1007/s11214-019-0599-5 doi: 10.1007/s11214-019-0599-5

Sitnov, M., & Schindler, K. (2010, apr). Tearing stability of a multiscale magnetotail current sheet. *Geophysical Research Letters*, *37*(8), 1–5. Retrieved from http://doi.wiley.com/10.1029/2010GL042961 doi: 10.1029/2010GL042961

Tedla, Y. T., Davis, G., & Arocho, R. (2018, may). Magnetospheric Multiscale (MMS) Mission: Surviving Extended Mission Long Eclipse. In *2018 spaceops conference*. Reston, Virginia: American Institute of Aeronautics and Astronautics. Retrieved from https://arc.aiaa.org/doi/10.2514/6.2018-2389 doi: 10.2514/6.2018-2389

Teste, A., Fontaine, D., Sauvaud, J.-A., Maggiolo, R., Canu, P., & Fazakerley, A. (2007, May). CLUSTER observations of electron outflowing beams carrying downward currents above the polar cap by northward IMF. *Annales Geophysicae*, *25*(4), 953–969. Retrieved 2023-06-13, from https://angeo.copernicus.org/articles/25/953/2007/ doi: 10.5194/angeo-25-953-2007

Tong, Y., Vasko, I., Mozer, F. S., Bale, S. D., Roth, I., Artemyev, A., … Torbert, R. B. (2018, nov). Simultaneous Multispacecraft Probing of Electron Phase Space Holes. *Geophysical Research Letters*, *45*(21), 11,513–11,519. Retrieved from https://onlinelibrary.wiley.com/doi/10.1029/2018GL079044 doi: 10.1029/2018GL079044

Torbert, R. B., Russell, C. T., Magnes, W., Ergun, R. E., Lindqvist, P.-A., LeContel, O., … Lappalainen, K. (2016, mar). The FIELDS Instrument Suite on MMS: Scientific Objectives, Measurements, and Data Products. *Space Science Reviews*, *199*(1-4), 105–135. Retrieved from http://link.springer.com/10.1007/s11214-014-0109-8 doi: 10.1007/s11214-014-0109-8

Tsyganenko, N. A. (1998, oct). Modeling of twisted/warped magnetospheric configurations using the general deformation method. *Journal of Geophysical Research: Space Physics*, *103*(A10), 23551–23563. Retrieved from http://doi.wiley.com/10.1029/98JA02292 doi: 10.1029/98JA02292

Tsyganenko, N. A., & Fairfield, D. H. (2004). Global shape of the magnetotail current sheet as derived from Geotail and Polar data. *Journal of Geophysical Research*, *109*(A3), A03218. Retrieved from http://doi.wiley.com/10.1029/2003JA010062 doi: 10.1029/2003JA010062

Ukhorskiy, A. Y., Sitnov, M. I., Merkin, V. G., Gkioulidou, M., & Mitchell, D. G. (2017, mar). Ion acceleration at dipolarization fronts in the inner magnetosphere. *Journal of Geophysical Research: Space Physics*, *122*(3), 3040–3054. Retrieved from https://onlinelibrary.wiley.com/doi/10.1002/2016JA023304 doi: 10.1002/2016JA023304

Usanova, M. E., & Ergun, R. E. (2022). Electron Energization by High-Amplitude Turbulent Electric Fields: A Possible Source of the Outer Radiation Belt. *Journal of Geophysical Research: Space Physics*(2015), 1–16. doi: 10.1029/2022ja030336

Wang, G. Q., Zhang, T. L., Wu, M. Y., Schmid, D., Cao, J. B., & Volwerk, M. (2019, jan). Solar Wind Directional Change Triggering Flapping Motions of the Current Sheet: MMS Observations. *Geophysical Research Letters*, *46*(1), 64–70. Retrieved from https://onlinelibrary.wiley.com/doi/abs/10.1029/2018GL080023 doi: 10.1029/2018GL080023

Wüest, M., Evans, D. S., & von Steiger, R. (2007). *Calibration of Particle Instruments in Space Physics* (M. Wüest, D. S. Evans, & R. von Steiger, Eds.). ESA Publications.

Xiao, S., Zhang, T., Ge, Y., Wang, G., Baumjohann, W., & Nakamura, R. (2016, feb). A statistical study on the shape and position of the magnetotail neutral sheet. *Annales Geophysicae*, *34*(2), 303–311. Retrieved from https://angeo.copernicus.org/articles/34/303/2016/ doi: 10.5194/angeo-34-303-2016

Yang, Y., Matthaeus, W. H., Roy, S., Roytershteyn, V., Parashar, T. N., Bandyopadhyay, R., & Wan, M. (2022, apr). Pressure–Strain Interaction as the Energy Dissipation Estimate in Collisionless Plasma. *The Astrophysical Journal*, *929*(2), 142. Retrieved from https://iopscience.iop.org/article/

10.3847/1538-4357/ac5d3e doi: 10.3847/1538-4357/ac5d3e

Zenitani, S., & Hoshino, M. (2005, jan). Relativistic Particle Acceleration in a Folded Current Sheet. *The Astrophysical Journal*, *618*(2), L111–L114. Retrieved from https://iopscience.iop.org/article/10.1086/427873 doi: 10.1086/427873

Zhang, T. L., Nakamura, R., Volwerk, M., Runov, A., Baumjohann, W., Eichelberger, H. U., … Fornacon, K.-H. (2005, nov). Double Star/Cluster observation of neutral sheet oscillations on 5 August 2004. *Annales Geophysicae*, *23*(8), 2909–2914. Retrieved from https://angeo.copernicus.org/articles/23/2909/2005/ doi: 10.5194/angeo-23-2909-2005

Zhou, X., Russell, C. T., Gosling, J. T., & Mitchell, D. G. (1997, jan). Three spacecraft observations of the geomagnetic tail during moderately disturbed conditions: Structure and evolution of the current sheet. *Journal of Geophysical Research: Space Physics*, *102*(A7), 14415–14424. Retrieved from https://onlinelibrary.wiley.com/doi/abs/10.1029/97JA00038 doi: 10.1029/97JA00038

Zimbardo, G., Greco, A., Sorriso-Valvo, L., Perri, S., Vörös, Z., Aburjania, G., … Alexandrova, O. (2010, oct). Magnetic Turbulence in the Geospace Environment. *Space Science Reviews*, *156*(1-4), 89–134. Retrieved from http://link.springer.com/10.1007/s11214-010-9692-5 doi: 10.1007/s11214-010-9692-5